Highly Efficient Visible-Light-Driven Photocatalytic Hydrogen Production of CdS-Cluster-Decorated Graphene Nanosheets

Qin Li,[†,‡] Beidou Guo,[†] Jiaguo Yu,[*,‡] Jingrun Ran,[‡] Baohong Zhang,[†] Huijuan Yan,[§] and Jian Ru Gong[*,†]

[†]National Center for Nanoscience and Technology, 11 Zhongguancun Beiyitiao, Beijing 100190, People's Republic of China

[‡]State Key Laboratory of Advanced Technology for Materials Synthesis and Processing, Wuhan University of Technology, Wuhan 430070, People's Republic of China

[§]Institute of Chemistry, The Chinese Academy of Science, Beijing 100080, People's Republic of China

ABSTRACT: The production of clean and renewable hydrogen through water splitting using photocatalysts has received much attention due to the increasing global energy crises. In this study, a high efficiency of the photocatalytic H_2 production was achieved using graphene nanosheets decorated with CdS clusters as visible-light-driven photocatalysts. The materials were prepared by a solvothermal method in which graphene oxide (GO) served as the support and cadmium acetate $(Cd(Ac)_2)$ as the CdS precursor. These nanosized composites reach a high H_2-production rate of 1.12 mmol h^{-1} (about 4.87 times higher

than that of pure CdS nanoparticles) at graphene content of 1.0 wt % and Pt 0.5 wt % under visible-light irradiation and an apparent quantum efficiency (QE) of 22.5% at wavelength of 420 nm. This high photocatalytic H_2-production activity is attributed predominantly to the presence of graphene, which serves as an electron collector and transporter to efficiently lengthen the lifetime of the photogenerated charge carriers from CdS nanoparticles. This work highlights the potential application of graphene-based materials in the field of energy conversion.
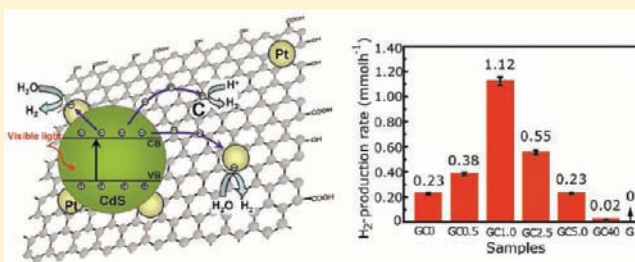
1. INTRODUCTION

The increasingly serious energy crisis and the environmental contamination caused by the burning of fossil fuels have led to an aggressive search for renewable and environmental-friendly alternative energy recourses.[1] Hydrogen energy has been recognized as a potentially significant alternative form of storable and clean energy for the future. Since the first report on photocatalytic splitting of water on TiO_2 electrodes was published in 1972 by Honda and Fujishima, photocatalysis has demonstrated wide-ranging potential applications in areas such as converting solar energy, recycling polluted water or air, and so on.[2−9] The research on the photocatalytic splitting of water to produce hydrogen, mimicking natural photosynthesis by converting solar energy into chemical energy, has been carried on extensively.[10−12] Recently, researchers have been focusing on the development of visible-light-responsive photocatalysts, because the ultraviolet (UV) light only accounts for about 4% of the solar radiation energy, while the visible light contributes to about 43%.[13−16]

As compared to their wide bandgap counterparts, chalcogenide nanomaterials, particularly CdS particles, are attractive photocatalytic materials for the conversion of solar energy into chemical energy under visible-light irradiation. Specifically, these materials have a conduction band edge sufficiently more negative than the reduction potential of protons and a relatively narrow bandgap, which can efficiently absorb visible light.[17,18] However, there are several issues that still limit the H_2-production rate on pure CdS particles. For example, the CdS particles tend to aggregate, forming larger particles, which results in a reduced surface area and a higher recombination rate of photoinduced electron−hole pairs. To solve these problems, many approaches have been proposed to enhance the photocatalytic activity of CdS particles, including the preparation of quantum-sized CdS,[19] deposition of noble metals,[20] preparation of heterogeneous semiconductors,[14] and incorporation of semiconductor particles in the interlayer region of layered compounds.[21] For example, Bard et al.[22] introduced CdS particles into colloidal suspensions of clay; Sato et al.[23] and Hirai et al.[24] incorporated CdS and/or ZnS particles into the interlayer of hydrotalcite and mesoporous silica, respectively. The layered structure of such a supporting matrix can efficiently suppress the growth of semiconductor particles as well as facilitate the transfer of the photogenerated electrons to the surface of photocatalysts. Furthermore, the recombination between the photoinduced charge carriers can be effectively suppressed, leading to the high efficiency of H_2 production.

There has been an explosion of interest in graphene since its discovery by Geim et al. in 2004 due to its potential applications in the physical, chemical, biological, photoelectric, and catalytic fields.[25] For example, Jiang et al.[26] synthesized graphene−CdS (G−CdS) nanocomposites by a reflux approach using thio salts as the sulphide source and hydrazine hydrate as the reducing

agent; Nethravathi et al.[27] prepared G—CdS/ZnS composites using H_2S gas as the sulphide source as well as reducing agent; Cao et al.[28] utilized a solvothermal method to synthesize a G—CdS nanocomposite material with good structural and optoelectronic properties, using dimethyl sulfoxide (DMSO) instead of H_2S. The solvothermal method not only avoids the use of toxic hydrazine hydrate, but also allows control over the degree of reduction of GO. In this way, the residual oxygen-containing hydrophilic groups on the graphene may allow the composite to be dispersed in water to a certain extent, which is required for the photocatalytic reaction.[29]

To the best of our knowledge, no previous work regarding the application of G—CdS on the photocatalytic H_2 production has been reported. However, the two-dimensional (2D) platform structure of graphene makes it an excellent supporting matrix for photocatalyst particles, similar to the role of layer-structured matrices played in improving the efficiency of the photocatalysts as mentioned above.[30] Moreover, because of the excellent electronic conductivity of graphene imparted by its 2D planar π-conjugation structure, it can effectively inhibit the recombination of the electron—hole pairs in the G—CdS nanocomposites.[31,32] In addition, an appropriate amount of graphene may darken the composites and thus enhance the absorption of visible light. In this work, the influence of graphene on the properties of the CdS clusters was systematically investigated, and high efficiency of the visible-light-driven photocatalytic H_2 production was achieved using the CdS-cluster-decorated graphene nanosheets as the photocatalyst. Furthermore, a mechanism for photocatalytic reaction in the graphene—CdS system is proposed.

2. EXPERIMENTS

2.1. Sample Preparation. The CdS-cluster-decorated graphene nanosheets (G—CdS) were prepared by a solvothermal method.[28] All of the reagents were of analytical grade and were used without further purification. Deionized (DI) water was used in all experiments. Graphene oxide (GO) was synthesized from natural graphite powder (>99.8%, Alfa Aesar) by a modified Hummers' method.[33] In a typical synthesis of the composite, a varying amount of the prepared GO and 1.6 mmol of $Cd(Ac)_2 \cdot 2H_2O$ (~98.5%, Aladdin) were dispersed in 160 mL of DMSO. The weight ratios of GO to $Cd(Ac)_2 \cdot 2H_2O$ were 0, 0.5%, 1.0%, 2.5%, 5.0%, and 40%, and the obtained samples were labeled as GC0, GC0.5, GC1.0, GC2.5, GC5.0, and GC40, respectively. Next, the homogeneous solution was transferred into a 200 mL Teflon-lined autoclave and held at 180 °C for 12 h after vigorous stirring and sonication. After that, the precipitates from the mixture were allowed to cool to room temperature and collected by centrifugation, and then rinsed with acetone and ethanol several times to remove the residue of DMSO. The final product was dried in an oven at 60 °C for 12 h. The bare graphene sample without any CdS clusters was prepared under the same experimental conditions for the purpose of comparison and was labeled as G.

2.2. Characterization. Powder X-ray diffraction (XRD) patterns were obtained on a D/MAX-2500 diffractometer (Rigaku, Japan) using Cu Kα radiation source (λ = 1.54056 Å) at a scan rate of 5° min^{-1} to determine the crystal phase of the obtained samples. The accelerating voltage and the applied current were 50 kV and 300 mA, respectively. The average crystallite sizes were calculated using the Scherrer formula (d = 0.9λ/B cos θ, where d, λ, B, and θ are crystallite size, Cu Kα wavelength, full width at half-maximum intensity (fwhm) in radians, and Bragg's diffraction angle, respectively). Scanning electron microscopy (SEM) images were collected on an S-4800 field emission SEM (FESEM, Hitachi, Japan). Transmission electron microscopy (TEM)
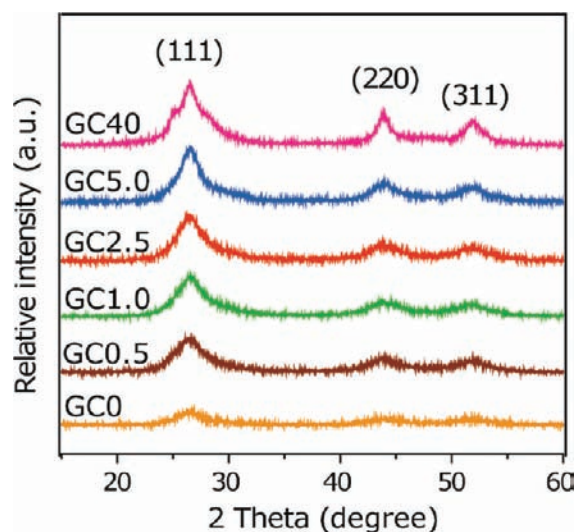
images, high-resolution transmission electron microscopy (HRTEM) images, and selected area electron diffraction (SAED) patterns were collected on an F20 S-TWIN electron microscope (Tecnai G2, FEI Co.), using a 200 kV accelerating voltage. The Brunauer—Emmett—Teller (BET) specific surface area (S_{BET}) of the powders was analyzed by nitrogen adsorption in a Micromeritics ASAP 2020 nitrogen adsorption apparatus (U.S.). All of the prepared samples were degassed at 180 °C prior to nitrogen adsorption measurements. The BET surface area was determined by a multipoint BET method using the adsorption data in the relative pressure (P/P_0) range of 0.05—0.3. The desorption isotherm was used to determine the pore size distribution using the Barret—Joyner—Halender (BJH) method, assuming a cylindrical pore modal. UV—vis diffused reflectance spectra of the samples were obtained from a UV—vis spectrophotometer (UV2550, Shimadzu, Japan). $BaSO_4$ was used as a reflectance standard. X-ray photoelectron spectroscopy (XPS) data were obtained by an ESCALab220i-XL electron spectrometer from VG Scientific using 300 W Al Kα radiation. The base pressure was about 3×10^{-9} mbar. The binding energies were referenced to the C 1s line at 284.8 eV from adventitious carbon. Atomic force microscopy (AFM) images were obtained by a Dimension 3100 AFM, operating in tapping mode with a scan rate of 1.20 Hz and a resolution of 256 × 256. An n-doped silicon tip with 1—10 Ω cm phosphorus (Veeco, MPP-11100-140) was used as the probe. Fourier transform infrared spectra (FTIR) of the samples were recorded between 500 and 2000 cm^{-1} on an IRAffinity-1 FTIR spectrometer.

2.3. Photocatalytic Hydrogen Production. The photocatalytic hydrogen production experiments were performed in a 100 mL Pyrex round-bottom flask, the openings of which were sealed with a silicone rubber septum, at ambient temperature and atmospheric pressure. A 350 W xenon arc lamp with a UV-cutoff filter (≥420 nm) was used as a visible light source to trigger the photocatalytic reaction and was positioned 20 cm away from the reactor. The focused intensity on the flask was ca. 180 mW cm^{-2}, which was measured by an FZ-A visible-light radiometer (made in the photoelectric instrument factory of Beijing Normal University, China) over the wavelength in the range of 400—1000 nm.[34]

In a typical photocatalytic experiment, 20 mg of the prepared G—CdS photocatalyst was dispersed with constant stirring in an 80 mL mixed solution of lactic acid (8 mL) and water (72 mL). A certain amount of $H_2PtCl_6 \cdot 6H_2O$ aqueous solution was dripped into the system to load 0.5 wt % Pt onto the surface of the photocatalyst by a photochemical reduction deposition method. Prior to irradiation, the system was bubbled with nitrogen for 30 min to remove the dissolved oxygen. During the whole reduction process, agitation of the solution ensured uniform irradiation of the G—CdS suspension. A 0.4 mL sample of the generated gas was collected intermittently through the septum, and hydrogen content was analyzed by gas chromatograph (GC-14C, Shimadzu, Japan, TCD, nitrogen as a carrier gas and 5 Å molecular sieve column). All glassware was rigorously cleaned and carefully rinsed with distilled water prior to use.

The apparent quantum efficiency (QE) was measured under the same photocatalytic reaction condition except that four 420 nm-LEDs (3 W) (Shenzhen LAMPLIC Science Co. Ltd., China) were used as light sources to trigger the photocatalytic reaction, instead of the xenon arc lamp. The LEDs were positioned 1 cm away from the reactor in four different directions, and the focused intensity on the flask for each of them was ca. 6.0 mW cm^{-2} over an area of 1 cm^2. The QE was calculated according to eq 1:[35]

$$QE\,[\%] = \frac{\text{number of reacted electrons}}{\text{number of incident photons}} \times 100$$

$$= \frac{\text{number of evolved } H_2 \text{ molecules} \times 2}{\text{number of incident photons}} \times 100 \quad (1)$$

Figure 1. XRD patterns of sample GC*x* solid powders (*x* = 0, 0.5, 1.0, 2.5, 5.0, and 40).

Table 1. Effects of Graphene Content on Physicochemical Properties and Quantum Efficiency (QE) of the Graphene–CdS Samples

samples	graphene content (wt %)	crystallite size[a] (nm)	S_{BET} (m² g⁻¹)	QE (%)
GC0	0	2.6	35.5	4.6
GC0.5	0.5	2.6	40.7	7.7
GC1.0	1.0	2.7	48.2	22.5
GC2.5	2.5	2.7	58.2	11.1
GC5.0	5.0	3.0	54.2	4.6
GC40	40	3.1	96.8	0.6

[a] Average crystallite size is determined by the broadening of the CdS (111) facet diffraction peak using the Scherrer formula.

Figure 2. SEM images of (a) sample GC0 and (b) sample GC1.0.

Figure 3. (a) TEM and (b) HRTEM images of sample GC1.0, with the inset of (b) showing the SAED pattern of graphene sheet decorated with CdS clusters.

3. RESULTS AND DISCUSSION

3.1. Phase Structures and Morphology. XRD patterns were recorded for the dried G–CdS powder to confirm the crystallographic phase of CdS in the composite and investigate the influence of graphene on the crystallinity of CdS nanoparticles. Figure 1 shows the XRD patterns of G–CdS nanocomposites synthesized with different contents of graphene as compared to that of the pure CdS (i.e., GC0). The peaks at 26.5°, 44.0°, and 52.1° correspond to the diffractions of the (111), (220), and (311) planes of cubic CdS (JCPDS 80-0019), respectively. The diffraction peaks are broad because the crystallite sizes of CdS nanoparticles in the samples are relatively small. In general, the solubility product constant (K_{sp}) for CdS particles is quite small, leading to fast nucleation and agglomeration of CdS nanocrystals.[13] However, DMSO can regulate the nucleation rate of CdS particles by slowly releasing S^{2-} ions into solution, resulting in a much smaller crystallite size. No characteristic diffraction peaks for carbon species are observed in the patterns because of the low amount and relatively low diffraction intensity of graphene. The XRD patterns also imply that graphene may enhance the crystallinity of CdS particles. As shown in Figure 1, pure CdS particles (GC0, yellow line) have poor crystallinity, perhaps because the reactor conditions are not ideal for their nucleation. After introducing 0.5% graphene, the XRD peaks of sample GC0.5 (brown line) become stronger and narrower due to the improved crystallinity of CdS particles. As the graphene content is increased, the intensity of XRD peaks is correspondingly enhanced. To further highlight this effect, the average crystallite sizes of different samples were calculated using the Scherrer formula for the (111) facet diffraction peak. As shown in Table 1, the average crystallite size of CdS particles increases from 2.6 to 3.1 nm. Thus, it can be deduced that the layer structure of graphene supplies a platform on which the CdS nanoparticles can nucleate, and thus graphene can promote the crystallization of CdS nanoparticles to a certain extent.

Furthermore, the morphologies of samples GC0 and GC1.0 were analyzed by SEM to directly observe the structure of the graphene nanosh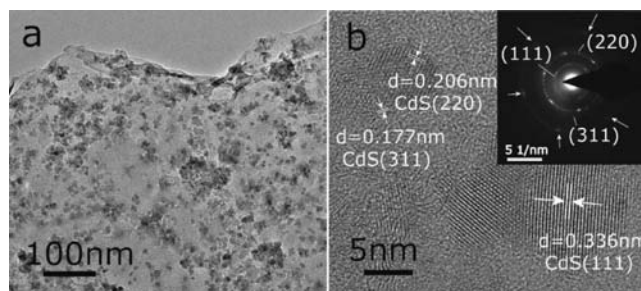eets decorated with CdS clusters, and to specifically investigate the influence of graphene on the morphology of the CdS clusters. The SEM micrograph in Figure 2a shows a significant aggregation of the CdS nanoparticles in sample GC0 and particle diameters of approximate 100 nm. However, Figure 2b shows that much smaller CdS clusters spread uniformly and tightly on the graphene sheets in sample GC1.0, indicating that graphene may interact with CdS nanoparticles and inhibit their aggregation. As has been reported previously, nanoparticles may interact with graphene sheets through physisorption, electrostatic binding, or charge transfer interaction,[36] and the exact mechanism is still under investigation.

The TEM image of GC1.0 (Figure 3a) shows that many small CdS particles are present on the graphene sheet, which has a characteristic wrinkle on the edge. The result further confirms the combination of graphene nanosheet and CdS clusters, which is consistent with the SEM image (Figure 2b). The HRTEM image (Figure 3b) shows that the size of the CdS clusters in GC1.0 is about 3 nm, which is in agreement with the value calculated by the Scherrer formula (Table 1). The lattice fringes
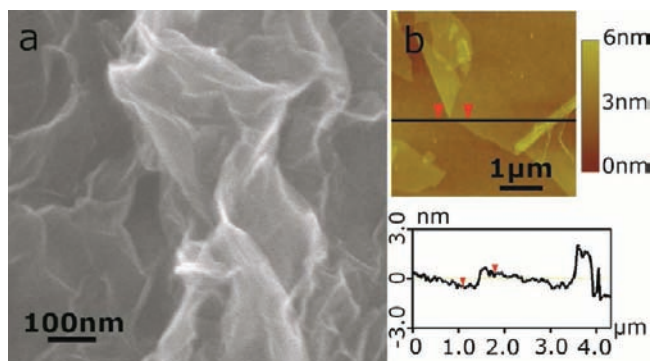
Figure 4. (a) SEM and (b) AFM images of GO sheets, with the inset of (b) showing that the thickness of the GO fragment is ca. 0.754 nm.

Figure 5. Nitrogen adsorption−desorption isotherms and corresponding pore size distribution curves (inset) of samples GCx solid powders (x = 0, 1.0, 5.0, and 40).

Figure 6. UV−vis diffuse reflectance spectra of samples GCx solid powders (x = 0, 0.5, 1.0, 2.5, 5.0, and 40).

of individual CdS clusters with d spacing of ca. 0.336, 0.206, and 0.177 nm can be assigned to the (111), (220), and (311) lattice planes of the cubic CdS, respectively. The selected area electron diffraction (SAED) pattern (inset in Figure 3b) indicates that these nanoparticles are polycrystalline. The three inside diffraction rings correspond to the (111), (220), (311) planes of the cubic CdS, which is fully consistent with the XRD results (Figure 1). In addition, the well-defined diffraction ring with six spots, five of which are indicated by the arrows in the SAED pattern, implies that thin, flat graphene films were obtained via the reduction of GO.

For comparison, the morphology of GO was also characterized by SEM and AFM. Unlike the nanocomposites, GO nanosheets without any CdS clusters have a crumpled shape in the SEM image (Figure 4a), suggesting that CdS clusters can prohibit the crumpling and agglomeration of graphene nanosheets during the solvothermal reduction process. The AFM image (Figure 4b) shows a 2D GO nanosheet with wrinkle-like features, and the apparent thickness is ca. 0.754 nm, which is comparable to the literature data (0.737 nm) for the single-layer GO nanosheet as reported before.[37]

3.2. BET Surface Areas and Pore Size Distributions. The effect of graphene on the BET surface area and pore structure of the prepared samples was investigated using adsorption−desorption measurements. As shown in Table 1, the BET surface area (S_{BET}) of samples gradually increases with increasing graphene content, from 35.5 to 96.8 m^2 g^{-1}. It should be noted that the specific surface area (m^2 g^{-1}) is expressed per gram of the samples, which contain some amount of carbon (graphene) with a low density. The planar density of graphene is 0.77 mg cm^{-2}, and the density of CdS is 4.82 g cm^{-3}. Consequently, the average densities of samples decrease with the increasing graphene, resulting in the increase of the S_{BET}. A greater specific surface area of photocatalysts can supply more surface active sites and make charge carriers transport easier, leading to an enhancement of the photocatalytic performance.[38] Thus, graphene may play a role in enhancing the photocatalytic activity.

Figure 5 shows the nitrogen adsorption−desorption isotherms and the corresponding curves of the pore size distribution (inset) for samples GC0, GC1.0, GC5.0, and GC40. According to the Brunauer−Deming−Deming−Teller (BDDT) classification, the majority of physisorption isotherms can be grouped into six types.[39] Typically, pure CdS (sample GC0) has an isotherm of type II, indicating the presence of large macropores, while samples GC1.0, GC5.0, and GC40 have isotherms of type IV,
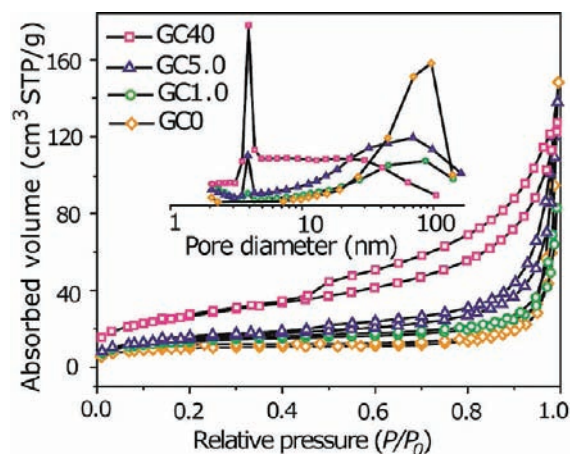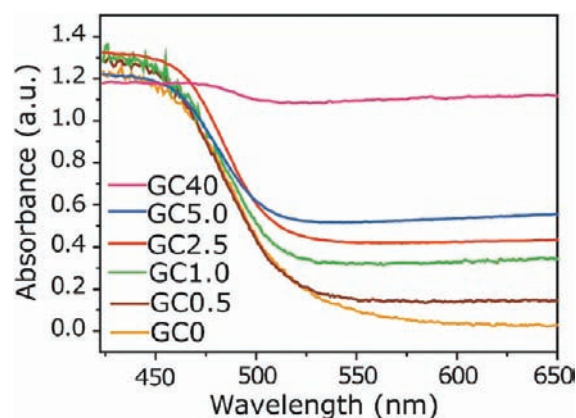
suggesting the presence of mesopores.[39] The shape of the hysteresis loops is of type H3, associated with slit-like pores formed by the aggregations of the plate-like particles. In other words, it appears that the prepared nanocomposite is composed of sheet-like graphene decorated with CdS clusters. The results are further confirmed by the corresponding pore size distribution. As shown in the inset of Figure 5, sample GC0 has macropores with a peak pore diameter of around 100 nm. When graphene is introduced, mesopores begin to appear in samples with a typical pore diameter of around 4 nm, and the amount of macropores decreases.

3.3. UV−Vis Diffuse Reflection Spectra. A comparison of the UV−vis diffuse reflectance spectra of samples GCx (x = 0, 0.5, 1.0, 2.5, 5.0, and 40) is displayed in Figure 6. There is an enhanced absorbance in the visible-light region (>500 nm) with increasing graphene content. This is also observed as a color change of the samples, which become darker, that is, from pale yellow to olive, when a low amount of black graphene was introduced into the pure CdS nanoparticles. The results show that the addition of graphene increases the absorbance of visible light. When the graphene content reaches 40% (sample GC40), the absorbance is significantly higher than that of the other samples used in this study. Because of the increased absorbance, a
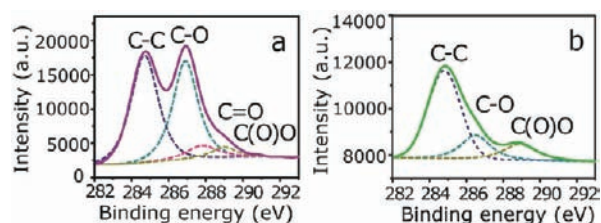
Figure 7. High-resolution XPS spectra of C 1s from (a) GO and (b) GC1.0.

Figure 8. FTIR spectra of (top) GC1.0 and (bottom) GO.

more efficient utilization of the solar energy can be obtained. Therefore, we can infer that the introduction of graphene in CdS particles is effective for the visible-light response of the composite.

3.4. XPS and FTIR Spectra. The hydrophilic groups on the surface of graphene, such as hydroxyl and carboxyl groups, can enhance the dispersion of graphene in water, providing the prerequisite for the H_2 generation occurring in aqueous solution. To investigate the degree of reduction of GO in the solvothermal reduction process, high-resolution XPS spectra of C1s were collected from samples GO and GC1.0 (Figure 7). The XPS spectrum of C1s from GO (Figure 7a, solid line) can be deconvoluted into four smaller peaks (dashed lines), which are ascribed to the following functional groups: sp^2 bonded carbon (C−C, 284.8 eV), epoxy/hydroxyls (C−O, 286.9 eV), carbonyls (C=O, 287.8 eV), and carboxyl (O−C=O, 288.9 eV),[40,41] indicating the high percentage of oxygen-containing functional groups. In comparison, in the XPS spectrum of C1s from GC1.0 (Figure 7b, solid line), the peak for C=O almost vanishes, and the peaks for C−O and O−C=O (dashed lines) still exist but with much lower intensities than those in GO, indicating the partial removal of the oxygen-containing functional groups. Furthermore, the degree of reduction of GO can be quantified by calculating the relative content of carbon in the samples. Briefly, GO has 48% graphitic carbon and 52% oxidized carbon, while 68% graphitic carbon and 32% oxidized carbon for GC1.0, respectively, showing the loss of oxygen-containing functional groups and the partial reduction of GO by the solvothermal reduction process. Thus, the graphene sheets in the composite can be dispersed in the aqueous solution to a certain extent.

Further evidence for the existence of the hydrophilic groups on the surface of graphene comes from FTIR spectra. In Figure 8, the characteristic bands of GO are observed at 972 cm^{-1} (epoxy stretching), 1057 cm^{-1} (alkoxy C−O stretching), 1224 cm^{-1} (phenolic C−OH stretching), 1402 cm^{-1} (carboxyl O−H stretching), and 1724 cm^{-1} (C=O stretching vibrations of carboxyl or carbonyl groups).[42] The peak at 1120 cm^{-1} is ascribed to C−O stretching vibrations of CO_2, and the broad absorption at 1624 cm^{-1} is related to H−O−H bending band of the adsorbed H_2O molecules or the in-plane vibrations of sp^2-hybridized C−C bonding.[33] As compared to the peaks of the functional groups of GO, sample GC1.0 has a similar spectrum but with much lower absorption intensity, especially for the peaks at 1224, 1402, and 1724 cm^{-1}, which are all assigned to the oxygen-containing functional groups. This result indicates the partial reduction of GO and is in good agreement with the XPS results.

3.5. Photocatalytic Activity and Tentative Mechanism of Photocatalytic Reaction. Recently, Zhang et al.[43] synthesized a graphene−TiO_2 nanocomposite and applied it as the
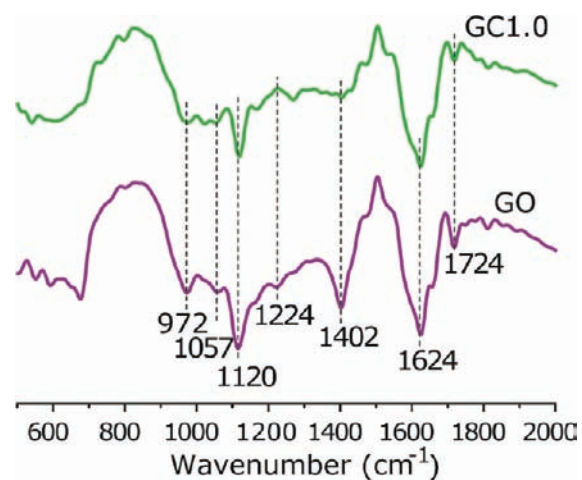
photocatalyst in hydrogen production from water splitting under irradiation of UV−vis light, obtaining a maximum H_2-production rate of 8.6 μmol h^{-1}. The results demonstrate that graphene is a very promising candidate for developing photocatalysts with high performance. However, because the bandgap of TiO_2 is wide and visible light cannot be utilized effectively, the efficiency of H_2 production is low. The applicability of chalcogenide nanomaterials has also been widely explored on hydrogen production. For example, Xu et al.[44] prepared $(Zn_{0.95}Cu_{0.05})_{1−x}Cd_xS$ solid solutions, which gave an H_2-production rate of 1.09 mmol h^{-1} when loaded with 0.75 wt % Pt; Bao et al.[13] synthesized nanoporous CdS nanostructures to increase the Pt loading content, and the maximum rate of H_2 production was 4.1 mmol h^{-1} with 13 wt % Pt.

In this work, photocatalytic H_2-production activity of the prepared graphene−CdS nanocomposites was evaluated under visible-light irradiation using lactic acid as a sacrificial reagent and Pt as a cocatalyst. The sacrificial reagent can prevent sulfide photocatalysts from the photocorrosion by providing sacrificial electron donors to consume the photogenerated holes, and Pt can reduce the overpotential in the production of H_2 from water and suppress the fast backward reaction (recombination of hydrogen and oxygen into water) as well.[45−47] Control experiments indicated that no appreciable hydrogen production was detected in the absence of either irradiation or photocatalyst, suggesting that hydrogen was produced by photocatalytic reactions on the photocatalyst.

Graphene exhibited a significant influence on the photocatalytic activity (Figure 9). Even with a small amount of graphene (0.5−2.5 wt %), the H_2-production rate was noticeably increased. For CdS alone (GC0), a relatively low photocatalytic H_2-production rate (0.23 mmol h^{-1}) was observed as expected due to the rapid recombination of conduction band (CB) electrons and valence band (VB) holes. In the presence of a small amount of graphene (0.5%), the activity of sample GC0.5 was slightly enhanced to 0.38 mmol h^{-1}, perhaps because the amount of graphene nanosheets was not large enough to efficiently disperse the CdS clusters. When the content was 1.0% (GC1.0), the H_2-production rate reached the highest value of 1.12 mmol h^{-1} with apparent quantum efficiency of 22.5% at 420 nm (Table 1). In this regard, the photocatalytic activity of sample GC1.0 exceeds that of GC0 by a factor of 4.87, and the
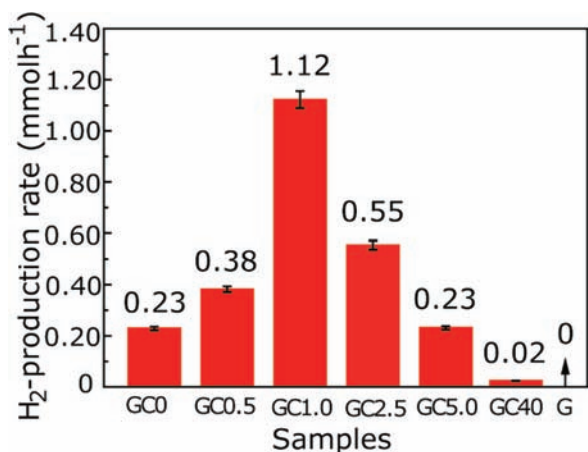
Figure 9. Comparison of the visible-light photocatalytic activity of samples GC0, GC0.5, GC1.0, GC2.5, GC5.0, GC40, and G for the H$_2$ production using 10 vol % lactic acid aqueous solution as a sacrificial reagent and 0.5 wt % Pt as a cocatalyst; a 350 W xenon arc lamp was used as the light source.
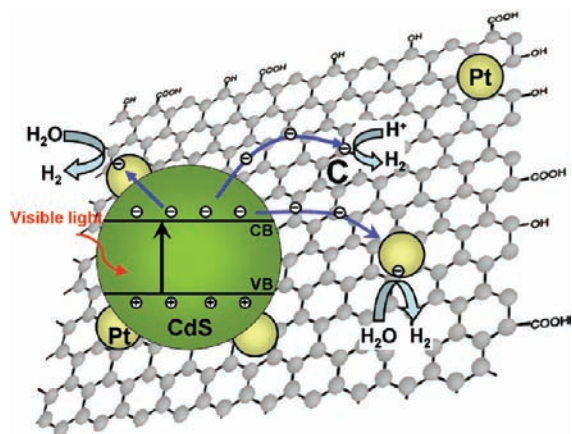
Figure 10. Schematic illustration of the charge separation and transfer in the graphene−CdS system under visible light. The photoexcited electrons transfer from the conduction band of semiconductor CdS not only to the located Pt, but also to the carbon atoms on the graphene sheets, which are accessible to protons that could readily transform to H$_2$.

H$_2$-production rate is significantly greater than that of most semiconductor photocatalysts. This is attributed to two factors: (1) As compared to the pure CdS counterpart (GC0), the larger specific surface area of GC1.0 offers more active adsorption sites and photocatalytic reaction centers, which favor an enhanced photocatalytic activity. (2) In the graphene−CdS system, graphene serves as an acceptor of the electrons generated in the CdS semiconductor and effectively decreases the recombination probability of the photoexcited electron−hole pairs, leaving more charge carriers to form reactive species. However, a further increase in the graphene content led to a deterioration of the catalytic performance. In particular, at the graphene content of 40% (sample GC40), the photocatalytic activity dramatically decreased, with an H$_2$-production rate of only 0.02 mmol h^{-1} and quantum efficiency of 0.6% at 420 nm (Table 1). It is reasonable because the introduction of a large percentage of black

graphene led to shielding of the active sites on the catalyst surface and also rapidly decreased the intensity of light through the depth of the reaction solution, which could be called a "shielding effect".[48] As a consequence, a suitable content of graphene is crucial for optimizing the photocatalytic activity of G−CdS nanocomposites. In comparison, no hydrogen was detected when sample G was used as the photocatalyst with Pt as a cocatalyst, suggesting that the bare graphene without CdS clusters is likely not active for photocatalytic H$_2$ production under the experimental conditions studied.

On the basis of the above results, a tentative mechanism of the photocatalytic reaction is proposed as illustrated in Figure 10. Under visible-light irradiation, electrons (e$^-$) are excited from the VB to the CB of the CdS semiconductor and then likely transfer in one of three following ways: (1) to Pt deposited on the surface of CdS clusters; (2) to carbon atoms on the graphene sheets; (3) to Pt located on the graphene nanosheets. Eventually, the electrons react with the adsorbed H$^+$ ions to form H$_2$. While the CB edge of CdS is more negative than the reduction potential of H$^+$/H$_2$, the H$_2$-production rate is negligible. This can be explained by the rapid recombination rate of CB electrons and VB holes. Once graphene is introduced to the CdS nanoparticles, it can serve as an electron collector and transporter to efficiently separate the photogenerated electron−hole pairs, effectively lengthening the lifetime of the charge carriers. Furthermore, the unique features of graphene allow photocatalytic reactions to take place not only on the surface of semiconductor catalysts, but also on the graphene sheet, greatly enlarging the reaction space.

4. CONCLUSIONS

A high efficiency of the photocatalytic H$_2$ production from water splitting under visible-light irradiation has been achieved over the graphene-CdS photocatalyst synthesized by a solvothermal method. Graphene nanosheets in the composite enhance the crystallinity and the specific surface areas of CdS clusters, and a low amount of graphene can dramatically improve the photocatalytic activity. The optimal weight percentage of graphene was found to be 1.0 wt %, which resulted in a high visible-light photocatalytic H$_2$-production rate of 1.12 mmol h^{-1} and corresponding apparent quantum efficiency of 22.5% at 420 nm with 0.5 wt % Pt as a cocatalyst. The results demonstrate that the unique features of graphene make it an excellent supporting material for semiconductor nanoparticles as well as an electron collector and transporter to separate photogenerated electron−hole pairs. This work not only demonstrated the potential of graphene as a support for CdS nanoparticles in photocatalytic hydrogen production, but also highlights more generally the potential application of graphene-based materials in the field of energy conversion.

■ AUTHOR INFORMATION

Corresponding Author
gongjr@nanoctr.cn; jiaguoyu@yahoo.com

■ ACKNOWLEDGMENT

■ REFERENCES

(1) Cortright, R. D.; Davda, R. R.; Dumesic, J. A. *Nature* **2002**, *418*, 964.

(2) Fujishima, A.; Honda, K. *Nature* **1972**, *238*, 37.

(3) Hoffmann, M. R.; Martin, S. T.; Choi, W.; Bahnemann, D. W. *Chem. Rev.* **1995**, *95*, 69.

(4) O'regan, B.; Grätzel, M. *Nature* **1991**, *353*, 737.

(5) Liu, S. W.; Yu, J. G.; Jaroniec, M. *J. Am. Chem. Soc.* **2010**, *132*, 11914.

(6) Bard, A. J.; Fox, M. A. *Acc. Chem. Res.* **1995**, *28*, 141.

(7) Park, J. H.; Kim, S.; Bard, A. J. *Nano Lett.* **2006**, *6*, 24.

(8) Šojić, D.; Despotović, V.; Abramović, B.; Todorova, N.; Giannakopoulou, T.; Trapalis, C. *Molecules* **2010**, *15*, 2994.

(9) Yang, H. G.; Liu, G.; Qiao, S. Z.; Sun, C. H.; Jin, Y. G.; Smith, S. C.; Zou, J.; Cheng, H. M.; Lu, G. Q. *J. Am. Chem. Soc.* **2009**, *131*, 4078.

(10) Zou, Z. G.; Ye, J. H.; Sayama, K.; Arakawa, H. *Nature* **2001**, *414*, 625.

(11) Tsuji, I.; Kato, H.; Kobayashi, H.; Kudo, A. *J. Am. Chem. Soc.* **2004**, *126*, 13406.

(12) Kudo, A.; Miseki, Y. *Chem. Soc. Rev.* **2009**, *38*, 253.

(13) Bao, N. Z.; Shen, L. M.; Takata, T.; Domen, K. *Chem. Mater.* **2008**, *20*, 110.

(14) Yan, H. J.; Yang, J. H.; Ma, G. J.; Wu, G. P.; Zong, X.; Lei, Z. B.; Shi, J. Y.; Li, C. *J. Catal.* **2009**, *266*, 165.

(15) Silva, L. A.; Ryu, S. Y.; Choi, J.; Choi, W.; Hoffmann, M. R. *J. Phys. Chem. C* **2008**, *112*, 12069.

(16) Li, Y. X.; Ma, G. F.; Peng, S. Q.; Lu, G. X.; Li, S. B. *Appl. Catal., A* **2009**, *363*, 180.

(17) Matsumura, M.; Furukawa, S.; Saho, Y.; Tsubomura, H. *J. Phys. Chem.* **1985**, *89*, 1327.

(18) Reber, J. F.; Rusek, M. *J. Phys. Chem.* **1986**, *90*, 824.

(19) Hoffman, A. J.; Yee, H.; Mills, G.; Yee, H.; Hoffmann, M. R. *J. Phys. Chem.* **1992**, *96*, 5546.

(20) Li, Y. X.; Xie, Y. Z.; Peng, S. Q.; Lu, G. X.; Li, S. B. *Chemosphere* **2006**, *63*, 1312.

(21) Shangguan, W. F.; Yoshida, A. *J. Phys. Chem. B* **2002**, *106*, 12227.

(22) Enea, O.; Bard, A. J. *J. Phys. Chem.* **1986**, *90*, 301.

(23) Sato, T.; Okuyama, H.; Endo, T.; Shimada, M. *React. Solids* **1990**, *8*, 63.

(24) Hirai, T.; Okubo, H.; Komasawa, I. *J. Phys. Chem. B* **1999**, *103*, 4228.

(25) Novoselov, K. S.; Geim, A. K.; Morozov, S. V.; Jiang, D.; Zhang, Y.; Dubonos, S. V.; Grigorieva, I. V.; Firsov, A. A. *Science* **2004**, *306*, 666.

(26) Wu, J. L.; Bai, S.; Shen, X. P.; Jiang, L. *Appl. Surf. Sci.* **2010**, *257*, 747.

(27) Nethravathi, C.; Nisha, T.; Ravishankar, N.; Shivakumara, C.; Rajamathi, M. *Carbon* **2009**, *47*, 2054.

(28) Cao, A. N.; Liu, Z.; Chu, S. S.; Wu, M. H.; Ye, Z. M.; Cai, Z.; Chang, Y. L.; Wang, S. F.; Gong, Q. H.; Liu, Y. F. *Adv. Mater.* **2010**, *22*, 103.

(29) Lerf, A.; He, H. Y.; Forster, M.; Klinowski, J. *J. Phys. Chem. B* **1998**, *102*, 4477.

(30) Meyer, J. C.; Geim, A. K.; Katsnelson, M. I.; Novoselov, K. S.; Booth, T. J.; Roth, S. *Nature* **2007**, *446*, 60.

(31) Shen, L.; Zeng, M. G.; Yang, S. W.; Zhang, C.; Wang, X. F.; Feng, Y. P. *J. Am. Chem. Soc.* **2010**, *132*, 11481.

(32) Eda, G.; Fanchini, G.; Chhowalla, M. *Nat. Nanotechnol.* **2008**, *3*, 270.

(33) Xu, Y. X.; Bai, H.; Lu, G. W.; Li, C.; Shi, G. Q. *J. Am. Chem. Soc.* **2008**, *130*, 5856.

(34) Yu, J. G.; Qi, L. F.; Jaroniec, M. *J. Phys. Chem. C* **2010**, *114*, 13118.

(35) Yu, J. G.; Zhang, J.; Jaroniec, M. *Green Chem.* **2010**, *12*, 1611.

(36) Williams, G.; Seger, B.; Kamat, P. V. *ACS Nano* **2008**, *2*, 1487.

(37) Dahn, J. R.; Sleigh, A. K.; Shi, H.; Reimers, J. N.; Zhong, Q.; Way, B. M. *Electrochim. Acta* **1993**, *38*, 1179.

(38) Yu, J. G.; Yu, H. G.; Cheng, B.; Zhou, M. H.; Zhao, X. J. *J. Mol. Catal. A* **2006**, *253*, 112.

(39) Sing, K. S.W.; Everett, D. H.; Haul, R.; Moscou, L.; Pierotti, R. A.; Rouquerol, J.; Siemieniewska, T. *Pure Appl. Chem.* **1985**, *57*, 603.

(40) Stankovich, S.; Piner, R. D.; Chen, X. Q.; Wu, N. Q.; Nguyen, S. T.; Ruoff, R. S. *J. Mater. Chem.* **2006**, *16*, 155.

(41) Stankovich, S.; Dikin, D. A.; Piner, R. D.; Kohlhaas, K. A.; Kleinhammes, A.; Jia, Y. Y.; Wu, Y.; Nguyen, S. T.; Ruoff, R. S. *Carbon* **2007**, *45*, 1558.

(42) Szabó, T.; Tombácz, E.; Illés, E.; Dékány, I. *Carbon* **2006**, *44*, 537.

(43) Zhang, X. Y.; Li, H. P.; Cui, X. L.; Lin, Y. H. *J. Mater. Chem.* **2010**, *20*, 2801.

(44) Zhang, W.; Zhong, Z. Y.; Wang, Y. S.; Xu, R. *J. Phys. Chem. C* **2008**, *112*, 17635.

(45) Alonso-Vante, N.; Colell, H.; Stimming, U.; Tributsch, H. *J. Phys. Chem.* **1993**, *97*, 7381.

(46) Bamwenda, G. R.; Tsubota, S.; Nakamura, T.; Haruta, M. *J. Photochem. Photobiol., A* **1995**, *89*, 177.

(47) Sakthivel, S.; Shankar, M. V.; Palanichamy, M.; Arabindoo, B.; Bahnemann, D. W.; Murugesan, V. *Water Res.* **2004**, *38*, 3001.

(48) Yu, J. G.; Ma, T. T.; Liu, S. W. *Phys. Chem. Chem. Phys.* **2011**, *13*, 3491.